

See discussions, stats, and author profiles for this publication at: <https://www.researchgate.net/publication/51546253>

Permeation of Styryl Dyes through Nanometer-Scale Pores in Membranes

ARTICLE *in* BIOCHEMISTRY · AUGUST 2011

Impact Factor: 3.02 · DOI: 10.1021/bi2006288 · Source: PubMed

CITATIONS

9

READS

23

6 AUTHORS, INCLUDING:



[Stephen Cheley](#)

University of Alberta

79 PUBLICATIONS 6,253 CITATIONS

[SEE PROFILE](#)



[Qiang Cui](#)

University of Wisconsin–Madison

200 PUBLICATIONS 13,520 CITATIONS

[SEE PROFILE](#)

Published in final edited form as:

Biochemistry. 2011 September 6; 50(35): 7493–7502. doi:10.1021/bi2006288.

Permeation of styryl dyes through nm-scale pores in membranes

Yao Wu[†], Liang Ma[‡], Stephen Cheley[§], Hagan Bayley[§], Qiang Cui[‡], and Edwin R. Chapman^{†,*}

[†]Howard Hughes Medical Institute and Department of Neuroscience, University of Wisconsin, Madison, WI 53706, USA

[‡]Department of Chemistry and Theoretical Chemical Institute, University of Wisconsin, Madison, WI 53706, USA

[§]Department of Chemistry, University of Oxford, Oxford OX1 3TA, England, UK

Abstract

Styryl dyes are widely used to study synaptic vesicle (SV) recycling in neurons; vesicles are loaded with dye during endocytosis and dye is subsequently released via exocytosis. During putative kiss-and-run exocytosis, the process of dye efflux from individual SVs has been proposed to occur via two sequential steps: dissociation from the membrane followed by permeation through a small fusion pore. To better understand the kinetics of dye efflux from vesicles during kiss-and-run events, we examined the efflux rates of different dyes through nm-scale pores formed in membranes by the toxins melittin and α -hemolysin; these pores approximate the size of fusion pores measured in neuroendocrine cells. We found that the axial diameter of each dye was a crucial determinant for permeation. Moreover, the two dyes with the largest cross-sectional areas were completely unable to pass through pores formed by a mutant α -hemolysin that has a slightly smaller pore than the wild-type toxin. The overall time constant for efflux (\sim s) of each dye was orders of magnitude slower than the time constant for dissociation from membranes (\sim ms). Thus, the permeation step is rate limiting and this observation was further supported by atomistic molecular dynamics simulations. Together, the data reported here help provide a framework to interpret dye destaining rates from secretory vesicles.

Keywords

FM dye; exocytosis; kiss-and-run; fusion pore; synaptic vesicle; molecular dynamics simulations

Secretion from neurons and neuroendocrine cells is a complex process that culminates in the fusion of secretory vesicles with the plasma membrane. Exocytosis proceeds through a crucial intermediate termed the fusion pore, in which a transient aqueous connection is formed between the vesicle lumen and the extracellular space. Once the fusion pore opens, it has been proposed that it has at least two fates, each of which gives rise to a distinct mode of secretion (1–4). In one case the pore dilates, resulting in the complete collapse of the vesicle into the plasma membrane, and this process is termed full fusion (5). In the other case, the

*CORRESPONDING AUTHOR: Howard Hughes Medical Institute, Department of Neuroscience, University of Wisconsin, 1300 University Avenue, SMI 129, Madison, WI 53706, chapman@physiology.wisc.edu, Tel: (608) 263-1762, Fax: (608) 265-5512.

SUPPORTING INFORMATION PARAGRAPH

A detailed method of expression and purification of mutant α HL, and additional figures. This material is available free of charge via the Internet at <http://pubs.acs.org>.

fusion pore is thought to undergo a reversal from the open state back to the closed state; this would occur without the complete merger of the vesicle and the plasma membrane, and is often referred to as “kiss-and-run” exocytosis (6). During kiss-and-run exocytosis, the small size of the fusion pore might limit the rate of secretion. Slow transmitter efflux rates could potentially drive receptor desensitization, rather than activation (2, 7), as evidenced by a recent study focused on cultured hippocampal neurons (8). In addition, detailed analysis of secretion from chromaffin cells revealed that kiss-and-run fusion pores act as “size exclusion” filters (9) by allowing the escape of smaller hormones whereas retaining larger hormones that can only be released via a subsequent full fusion event.

Kiss-and-run events are well established for large dense-core vesicle (LDCV) exocytosis in neuroendocrine cells and cell lines and have been studied in detail via carbon fiber amperometry (4, 10–12) and capacitance measurements (2, 13–15). However, whether kiss-and-run occurs during SV exocytosis in neurons has been a subject of debate (8, 16–22) although recent experiments, using quantum dots, have provided direct and compelling evidence for kiss-and-run exocytosis in hippocampal neurons (23). The emerging consensus is that kiss-and-run occurs in central synapses, but whether this is a common or relatively rare mode of exocytosis remains unclear and is likely to depend upon the specific synapse under study.

The lipophilic styryl dye FM1–43, along with a number of structurally related variants that comprise the FM dye family, are widely used to study endo- and exocytosis of recycling SVs in intact neurons (1, 7, 8, 16, 17, 24). The dramatic increase in the fluorescence of these dyes that occurs when they bind to membranes can serve as an index of how much dye is incorporated into the membrane (25). Hence, these dyes provide a quantitative tool to study vesicle dynamics in presynaptic nerve terminals. The rate and extent of dye loss from vesicles undergoing exocytosis can, in principle, be used to determine the mode of exocytosis.

A study by Richards et al. (7) suggested a simple pore permeation model for small, slow dye destaining events - interpreted to be kiss-and-run - of FM1–43 escaping from individual SVs in hippocampal boutons. This process can be viewed as two sequential steps: (1) membrane bound dye molecules dissociate from the lipid membrane and (2), free dye molecules within the vesicle lumen permeate through the open fusion pore (7). Since our previous studies (7, 25) revealed that all members of the FM dye family depart from membranes at rates (time constants in the ms range) that are orders of magnitude faster than their overall destaining rates from presynaptic nerve terminals (time constants in the seconds range) (1, 7, 26), we suggested that the second step - permeation - was rate-limiting. If the pore is on the order of 1–2 nm, as it is in some neuroendocrine cells (2, 4, 10, 13, 21, 27–29), the size of the dye, relative to the size of the pore, is likely to represent a crucial parameter that determines the efflux rate. Hence, under conditions of full fusion, different dyes would be expected to exhibit similar destaining rates, whereas during kiss-and-run, smaller dyes would be expected to more readily leave vesicles (via nm-scale fusion pores) as compared to those with larger axial cross-sectional areas.

An earlier study employed melittin to empirically determine the kinetics of FM1–43 efflux through small pores in membranes (7). Even though the structure(s) of melittin pores have not been definitively determined, a number of studies suggest that this pore is toroidal and might be lined - at least partially - with lipids (30). There are two hypothesized models for the structure of secretory vesicle fusion pores: the lipidic pore and the protein-lined pore (13, 27); thus, melittin simulates aspects of the lipidic fusion pore. However, we note that the diameter of melittin pores is somewhat heterogeneous and this parameter varies as a function of [melittin] (31, 32), and melittin pores are only ~4 nm long (33) as compared to

fusion pores in cells which must initially span two bilayers. So, to address these concerns, and to generate pores that simulate putative protein-lined fusion pores during kiss-and-run exocytosis (34), we also utilized α -hemolysin (α HL), which forms longer proteinaceous pores whose structure has been determined at atomic resolution (35). By measuring the efflux rates of different dyes through both kinds of pores *in vitro*, we gained a detailed understanding of how sensitive dye permeation rates are to pore diameter. Finally, our empirical findings were bolstered by complementary molecular dynamics (MD) simulations in which the free energy, and diffusion constant profiles, for FM1–43 permeation through wild-type and mutant α HL pores, were computed. These data were then used to estimate the translocation time of FM1–43 through these pores, based on a mean first passage time analysis.

MATERIALS AND METHODS

Dyes

FM1–84, FM1–43, and FM2–10 were obtained from Invitrogen (Carlsbad, CA). SynaptoGreen C3 and SGC5 were synthesized by F. Mao (Biotium, Inc.). The structure of each dye is shown in Figure S1 of the Supporting Information.

Expression and purification of wild type and mutant α HL

Wild-type α HL was expressed, purified, and assembled into heptamers as described previously (36). The pT7- α HL-M113W (α HL RL2) plasmid was generated by mutating the α HL RL2 gene in a pT7 vector (37) (see Supporting Information for details).

Liposomes

1,2-Dioleoyl-sn-glycero-3-phosphoethanolamine (PE) and 1,2-dioleoyl-sn-glycero-3-phosphocholine (PC) were from Avanti Polar Lipids (Alabaster, AL). Lipids, stored in chloroform, were dried under a stream of nitrogen, and then subjected to vacuum for one hour. Dye-containing liposomes were made by re-suspending the dried lipid film (30% PE/70% PC) in HEPES buffer (50 mM HEPES and 100 mM NaCl, pH 7.4) plus dye, followed by extrusion using a 100 nm filter, resulting in dye-loaded liposomes with a mean diameter of 130 nm.

Measurement of dye efflux rates through pores

FM dye-containing liposomes were incubated with melittin (Sigma, MO) at melittin/lipid ratios of 1:10, 1:20, and 1:800 for 5 min in the presence of “external” dye, as described in a previous study (7), to allow melittin pores to form without loss of trapped dye. The liposome•FM dye mixtures were first diluted by hand and changes in fluorescence intensity were monitored using a PTI QM-1 spectrophotometer (South Brunswick, NJ). After optimization of toxin/lipid ratios, dye efflux was time resolved using an Applied Photophysics SX 18 MV stopped-flow spectrometer (Leatherhead, Surrey, United Kingdom) at room temperature as described previously (25). The fluorescence changes were well fitted by single exponential functions using GraphPad Prism 3 (La Jolla, CA). Rates are reported as time constants.

To produce pores with different structures and diameters, we also utilized wild-type and a M113W mutant form of α HL (37), at toxin to lipid molar ratios of: 1:14, 1:50 and 1:300. To form pores, toxins and vesicles were incubated for 1 h at 37 °C; experiments were then carried out at room temperature. We examined dyes that, as shown in a previous study (7, 25), yield strong fluorescence signals; these dyes are: FM1–43 (4 μ M), FM1–84 (4 μ M), SynaptoGreen C3 (30 μ M), FM2–10 (50 μ M), and SGC5 (2 μ M) (25).

System setup for MD simulations

The crystal structure of wild-type α HL (PDB code 7AHL (35)) was taken as the starting structure for all simulations. Hydrogen atoms were added to the crystal structure with the HBUILD module (38) in the CHARMM program (39) to create an all-atom model. To generate a model for the M113W mutant, residue Met113 on each of the seven subunits of the wild-type structure was replaced with a tryptophan (Trp). Before MD simulations, the protein was first reoriented such that the longest dimension lied along the z direction and the center of mass (COM) of the transmembrane region was at $z = 0$ nm (see Figure 4A). After the reorientation, the diffusion pore ranged from $z \sim -2.0$ to 8.0 nm, with a total length $L \sim 10.0$ nm (35); residue M113 was at $z \sim 2.0$ to 2.5 nm.

The protein atoms were described with the all-atom CHARMM 27 (40) force field. For FM1–43, a force field was constructed by recommended procedures for CHARMM force field development; i.e., force field parameters from chemically similar groups in CHARMM 27 were used. Specifically, parameters for amine groups were adopted from those of lipid headgroups; parameters for the six-member ring containing nitrogen were adopted from those of NADP molecule; parameters for the benzene ring and ethylene group were available in CHARMM 27. This scheme ensured compatibility between parameters for FM1–43 and those for protein and water. All bonds involving hydrogen atoms were constrained using the SHAKE algorithm (41) to allow a time step of 2 fs.

Due to the large size of α HL, only part of the system was allowed to move during the simulation, which is justified because diffusion of FM1–43 does not directly implicate a large number of protein atoms. Depending on the range of z , either the generalized boundary solvent potential (GSBP) (42, 43) or an implicit solvent method GBSW (44) was applied to treat long-range electrostatic interactions.

For the region with z between -2.0 and 4.1 nm, the diffusion pore was relatively narrow, and a GSBP setup was applied. The system was partitioned into two regions: a rectangular inner region with x , y and z dimensions of 3.6 , 3.6 and 10.0 nm, respectively, and the remaining portion of the system as the outer region. The z of the inner region ranged from -4.0 to 6.0 nm (as shown in Figure 4A), and was solvated with explicit water molecules described with the modified TIP3P model (45). All atoms in the inner region were subjected to a weak GEO type of restraining potential to keep them inside the inner rectangular box with the MMFP module of CHARMM; the effect of restraint on most inner region atoms was negligible and only significant to those within 0.2 nm from the inner/outer boundary. The outer region atoms were fixed during the simulations. The static field due to the outer region atoms and the reaction field matrix for the inner region atoms were evaluated with the linear Poisson-Boltzmann approach using a focusing scheme. In the Poisson-Boltzmann calculations, the dielectric constant of the protein and implicit membrane (treated as a dielectric slab) was set to be 1, with a value of 80 for water; the salt concentration was set to be 0 M. The optimized radii of Roux and Nina (46, 47) were adopted to define the solvent-protein dielectric boundary. NVT simulations were carried out with the temperature controlled using the Nose-Hoover scheme (48, 49).

For the region with z between 3.8 to 8.0 nm, the diffusion pore was relatively wide, and an implicit solvent model GBSW (44) was applied. Protein atoms more than 1.4 nm away from the dye were fixed during the simulations, which were Langevin dynamics coupled to a thermal bath at 300K with a friction coefficient γ of 10 ps^{-1} . The dielectric map and salt concentrations in the GBSW setup were the same as those in the GSBP setup.

Estimating the axial diameters of FM dyes

Geometries were first optimized in the gas phase with an approximate density functional method (SCC-DFTB, ref. (50)). The optimized structures were then simulated in the gas phase with SCC-DFTB using Nose-Hoover molecular dynamics at 300K for 100 ps. The last 80 ps trajectories were used to obtain averaged structures of the dye molecules; the axial diameter for each dye was estimated based on moments of inertia calculations for the average structure, augmented by the van der Waals radii for carbon atoms. The estimated axial diameters, at the thickest point of each dye, were, in nm: FM1–84, 1.16; FM1–43, 1.10, SGC3, 1.04, and FM2–10, 1.03; the standard deviation in each case was 0.02 nm. These structures are shown in Figure S2 of the Supporting Information.

Free energy simulations

Umbrella sampling was employed to compute the one-dimensional free energy profiles $W(z)$ for the translocation of FM1–43 through the diffusion pore along the z direction. The umbrella potential was applied to the z coordinate of the COM of FM1–43, and the force constant was 200 kcal/(mol•nm²). In total, more than 100 windows were used to cover the range of z between –2.0 and ~8.0 nm. The Weighted Histogram Analysis Method (WHAM) (51, 52) was used to obtain $W(z)$.

For the region with z between –2.0 and 4.1 nm (with the GSBP setup), long simulations were performed to ensure sufficient convergence of $W(z)$ since the limiting barrier of $W(z)$ fell in this region. For each window, 1 ns equilibration simulation was carried out before 1.3 ns of production run. To monitor convergence of $W(z)$, results using the entire 1.3 ns data were compared with those using only the first 500 ps of the production run (see Results).

For the region with z between 3.8 and 8.0 nm (with the GBSW setup), shorter simulations were carried out since as shown below, the fine details of $W(z)$ in this region did not affect the overall translocation time. For each window, 300 ps equilibration simulation was carried out followed by 500 ps production run. To monitor convergence of $W(z)$, results using the entire 500 ps data were compared with those using only the first 300 ps of the production run (see Results).

Calculation of translocation time

The translocation time of FM1–43 was estimated based on the mean first passage time, which was calculated based on $W(z)$ (53, 54):

$$t = \int_0^L dz e^{W(z)/k_B T} D(z)^{-1} \int_0^z dz' e^{-W(z')/k_B T} \quad (1)$$

where $L \sim 10.0$ nm was the length of the pore, k_B the Boltzmann constant, and T the absolute temperature. $D(z)$ was the z -dependent diffusion constant, which could be extracted from the umbrella sampling simulations based on an analysis of the velocity autocorrelation function in the framework of the Generalized Langevin Equation (GLE) (55). In the current simulations, $D(z)$ was found to be largely z -independent and a uniform value of 7.0 nm²/ps was used.

RESULTS

Styryl dye efflux from vesicles through nanometer-scale pores

In the current study we have focused on FM1–84, FM1–43, SynaptoGreen C3 and FM2–10 which share an identical fluorophore core; their only structural differences lie in the length

of their lipophilic tails. Since the tails are branched, longer tails give rise to larger axial diameters; these values were estimated as described in Methods (see also Figure S1 and S2 of the Supporting Information for dye structures). In addition, we characterized another, new, lipophilic fluorescent dye, SGC5, which has a structure that is distinct from the styryl dyes. SGC5 gives rise to good signal/noise ratios and might prove useful for single vesicle destaining experiments (25).

To begin to understand the factors that influence the kinetics of dye efflux through fusion pores, we made use of pores formed in artificial liposomes (30% PE/70% PC) by first using melittin (7). Melittin is a toxin peptide, produced by honeybees, that forms pores with average diameters of ~1.3–2.4 nm in membranes; these pores are likely to be partially or completely lipidic (30, 31). Artificial liposomes were formed in the presence of dye molecules such that dye was bound to both the internal as well as the external leaflets of the bilayer. To allow pores to become fully formed, the liposomes were incubated with melittin for 5 minutes at room temperature. Dye-containing liposomes were then rapidly diluted in buffer and the loss of fluorescence was monitored using a spectrofluorometer (Figure 1A). One component of the decrease in the fluorescence signal was due to the dissociation of dye molecules from the external leaflet of the liposomes. This occurred rapidly, on the ms timescale (7, 25), which made it too fast to be detected in these hand mixing experiments. The second, slower, component was due to loss of dye molecules from the inside of the liposome; these dye molecules are likely to first depart from the interior membrane followed by permeation through the nm-scale pores formed by melittin, which occurred on the seconds timescale (Figure 1A). However, we note that some degree of lateral diffusion of the dyes, through the potentially lipidic melittin pores, cannot be ruled out.

The first goal was to find conditions in which liposomes harbor, on average, a single pore, so that the efflux rates through individual pores could be determined. To this end, we titrated melittin onto dye-loaded vesicles. When the melittin/lipid ratio was increased from 1:800 to 1:20, there was a greater loss of fluorescence, presumably due to the formation of pores in all liposomes when more melittin was used (Figure 1B). This conclusion was supported by the finding that the loss of fluorescence reached a limit and no further drop was observed at a ratio of 1:10 (Figure 1B); hence, a melittin/lipid ratio of 1:20 should be sufficient to induce pore formation in virtually every liposome. At a melittin/lipid ratio of 1:800, one-half of the total fluorescence signal was lost (Figure 1B) indicating that roughly 50% of the liposomes harbored one pore with the other 50% of vesicles devoid of pores (assuming efficient mixing of melittin and liposomes, and assuming that the pores do not associate with one-another). We then examined the kinetics of dye efflux under these conditions (melittin/lipid ratio of 1:800) in stopped-flow spectrometer, using each of the five dyes. With melittin, the efflux rates of FM1–84 and SGC5, which possess relatively long 5-carbon tails, were significantly slower than those of the other three smaller dyes. Interestingly, the three smaller dyes, FM1–43, SyGC3, and FM2–10, all exhibited similar efflux kinetics (Figure 1, Table 1). These data confirm an earlier study focused on FM1–43 (7), and also indicate the existence of a critical threshold regarding the relative diameters of the dyes relative to the pore during permeation, as detailed further below and in the Discussion.

While these results are consistent with an earlier study of FM1–43, it is important to note that the stoichiometry of melittin pores remains unclear and is thought to be variable; indeed, pore size depends on the concentration of melittin used (30–32). To address these concerns, we turned to α HL, as a proteinaceous pore. α HL is a 33.2 kDa water soluble monomer that forms reproducible and fixed-stoichiometry heptameric pores. The crystal structure of the α HL pore has been determined and the most narrow segment of the pore lumen has a diameter of 1.4 nm (Figure 2A) (35). To retard the efflux of dyes, Trp residues were introduced into the neck of the pore lumen, at residue M113, where the narrow

segment is located (Figure 2A). It has been confirmed that the conductance of this M113W mutant form of α HL (α HL-M113W) pore is ~20% lower than that of wild-type α HL (α HL-wt) (37).

We carried out the same experiments as described for each dye and melittin, but using α HL-wt and α HL-M113W. As detailed in Experimental Procedures, the incubation time for wild-type and mutant α HL was 1 hour at 37 °C to ensure complete pore formation. The α HL/lipid ratios for a 50% loss of fluorescence were 1:300, and so this condition, in which half the vesicles have a single pore, was used in all time resolved stopped-flow experiments (Figure 2 and 3). As with melittin pores, the efflux of FM1-84 and SGC5 through α HL-wt was significantly slower than the other three dyes, whereas FM1-43, SynaptoGreen C3 and FM2-10 exhibited similar efflux rates (Figure 2, Table 1). The time constant for efflux of FM1-43 was 7.9 s, which was in line with the time constant for destaining of FM1-43 from single SVs ($\tau = 7.2$ s) during putative kiss-and-run events in cultured hippocampal neurons (7). FM1-43, SynaptoGreen C3 and FM2-10 efflux through α HL-M113W pores was much slower than through α HL-wt pores, and the efflux rates of these three dyes now differed from one-another (Figure 3, Table 1). These data again indicate that the size of the dye, relative to the size of the pore, plays a crucial role in determining the rate of efflux. This point is further underscored by the finding that FM1-84 and SGC5 failed to permeate through the smaller pores composed of α HL-M113W (Figure 3D, E).

Pores formed by α HL are similar in size to fusion pores in neuroendocrine cells (2, 4, 10, 13, 21, 27–29), and both kinds of pores are similar to the axial cross sectional area of the styryl dyes. This coincidence, coupled to the empirical efflux rates measured above, demonstrate that styryl dye flux from secretory vesicles will be sensitive to the dimensions of cellular fusion pores.

Free energy profiles and translocation times of FM1-43 through wild-type and M113W mutant α HL-wt as determined from simulations

To further analyze the influence of dye size on flux rates through nm-scale pores we carried out MD computer simulations for the free energy profiles for FM1-43 in α HL pores to estimate the translocation time. First, we checked the consistency of free energy profiles $W(z)$ calculated using GSBP (42, 43) and GBSW (44) set-ups by comparing $W(z)$ values in the overlapping region, i.e., z between 3.8 and 4.1 nm. As shown in Figure 4B, wild-type $W(z)$ in the overlapping region using the two methods were consistent with each other. This justified connecting $W(z)$ from the two sets of simulations to generate the complete $W(z)$ profile across the entire range of interest. $W(z)$ for α HL-M113W showed similar behavior (data not shown).

The computed $W(z)$ for α HL-wt and α HL-M113W are shown in Figure 4C. For both systems, there were two barriers in $W(z)$ and the limiting barrier was observed around the narrowest segment of the pore, $z \sim 2.0$ to 2.5 nm, where the M113 residues (or W113 in the M113W mutant) were located. The limiting barrier was ~14 kcal/mol for α HL-wt and it increased to ~15 kcal/mol for α HL-M113W. Since both Met and Trp are charge neutral residues, the change of $W(z)$ is due mainly to the larger size of the Trp residues.

Next, the convergence of $W(z)$ with respect to sampling was evaluated by comparing $W(z)$ using different lengths of production runs. As shown in Figure S3 of the Supporting Information, $W(z)$ in the GSBP region had largely converged whereas $W(z)$ in the GBSW region still showed variation on the order of 2–3 kcal/mol as simulation time was extended. However, as discussed below, the fine details of $W(z)$ in the GBSW region were not essential to the overall translocation time. In other words, the calculated $W(z)$ profiles have converged to a satisfactory degree for the current purpose.

The calculated dye translocation times according to Eq. 1 were ~1.3 s and ~12.7 s for α HL-wt and α HL-M113W, respectively. Encouragingly, these values agreed with experimental values of ~8 s and ~35 s, within the same order of magnitude.

To investigate the sensitivity of the calculated translocation time to the height of the second barrier in the GBSW region, we first fitted the wild-type $W(z)$ with two Gaussian functions (see Figure 5A for the fit):

$$W_{fit}(z) = h_1 e^{-\frac{(z-z_1)^2}{2\sigma_1^2}} + h_2 e^{-\frac{(z-z_2)^2}{2\sigma_2^2}} \quad (2)$$

where $h_1=14.08$ kcal/mol, $z_1=1.5$ nm, $\sigma_1=1.5$ nm, $h_2=8.0$ kcal/mol, $z_2=6.0$ nm and $\sigma_2=0.8$ nm for the best fit of the computed translocation time. We then fixed $h_1=14.08$ kcal/mol and calculated the ratio t/t_0 for different h_2 , where t_0 was the calculated translocation time with $h_2=8.0$ kcal/mol. As shown in Figure 5B, t/t_0 was nearly 1 for $h_2 \leq 14$ kcal/mol. This confirms the expectation that the translocation kinetics are not sensitive to the height of the second (lower) barrier. Consistent with this simple test using Gaussian functions, t values were calculated for the $W(z)$ profiles in Figure S3 of the Supporting Information based on different lengths of production runs. The values were 1.7 s and 1.3 s for α HL-wt and 10.7 s and 12.7 s for α HL-M113W, once again confirming that calculated translocation time was insensitive to the lower barrier and the $W(z)$ had sufficiently converged for the current purpose.

DISCUSSION

To gain a better understanding of how FM dyes - and SGC5 - are released from presynaptic nerve terminals, we simulated putative kiss-and-run fusion pores using toxins in artificial liposomes and directly measured dye efflux rates. The structure of melittin pores remain somewhat unclear but are generally thought to be toroidal with at least partial lipidic nature with a pore diameter that ranges from 1.3 to 2.4 nm (30, 31), and were thus used to simulate lipidic fusion pores. α HL, which assembles into heptamers that form protein-lined pores in membranes - with a uniform and well-defined structure (Figure 2A) (35) - were used to simulate proteinaceous fusion pores. The length of the α HL pore is 10 nm, and the diameter ranges from 1.4 nm at the narrowest point up to 4.6 nm at the widest point. The effective diameter is 1.14 nm, as estimated from conductance measurements of single heptamers (56). Moreover, to probe the relationship between pore diameter and dye flux rates in deeper detail, we also examined a mutant form of α HL in which a ring of seven pore lining residues (M113) at the neck of the pore lumen, were replaced by Trp residues (Figure 2A). The conductance of the α HL-M113W pore was ~20% lower than that of α HL-wt (37), indicating that the effective diameter of α HL-M113W pore is ~1 nm.

The time constants for efflux of FM1-43 through melittin and α HL-wt pores were 8.4 and 7.9 s, which were comparable to the time constant for FM1-43 destaining from single SVs ($\tau = 7.2$ s) during putative kiss-and-run events in cultured hippocampal neurons ((7), but see also (16)). For both melittin and α HL-wt pores, the two largest dyes - FM1-84 and SGC5 - exhibited the slowest efflux rates as compared to the other three smaller dyes. Interestingly, FM1-43, SynaptoGreen C3, and FM2-10 exhibited similar efflux rates through α HL-wt pores (Table 1). It is possible that the 5-carbon tails of FM1-84 and SGC5 have reached a critical cross-sectional area, resulting in a significantly larger energy barrier that must be overcome to pass through the α HL-wt pore. Indeed, the small reduction in pore diameter in α HL-M113W pores was sufficient to prevent passage of FM1-84 and SGC5 (Figure 3D, E). Moreover, the efflux rates of the three smaller dyes were not only markedly slower through the mutant pore than through wild-type pores, they now differed from one-another (Table 1).

These results indicate that biological fusion pores with diameters of 1–2 nm (2, 4, 10, 13, 21, 27–29) are, by chance, of similar dimensions to the axial cross sectional area of the FM dyes (which we estimate to be, in nm: FM1–84, 1.16; FM1–43, 1.10, SGC3, 1.04, and FM2–10, 1.03; see Methods for details). Hence, small changes in the diameter of the dyes, or in the diameter of the fusion pore, result in large changes in the dye efflux rates.

It should be noted that lipophilic components in the synaptic cleft might also influence the destaining kinetics of these dyes from neurons. Furthermore, there is a possibility that the dyes may leave secretory vesicles in cells via lateral diffusion along lipidic pores, which might influence the kinetics of permeation. However, the data reported here demonstrate that the efflux kinetics through melittin or α HL pores are similar, so this possibility does not appear to strongly affect our conclusions.

To gain a more detailed understanding of efflux, we also studied the translocation of FM1–43 in α HL-wt and α HL-M113W pores using MD computer simulations. We computed the free energy profiles of FM1–43 translocation in the pore, from which the translocation times were calculated based on mean first passage time. The calculated results were in agreement (within one order of magnitude) with the empirical efflux rates. Comparing the free energy profiles for α HL-wt and α HL-M113W, we confirmed that the bulky side chain of the Trp mutation increased the energetic barrier for FM1–43 diffusion, which lead to the observed change in translocation time and efflux rate, again highlighting the importance of pore size when it approaches the diameter of the dye used to study flux.

Taken together, these findings indicate that the size of the dye, relative to the size of the pore, is a crucial determinant for efflux rates through kiss-and-run fusion pores; our data strongly suggest that permeation (the second step) is the rate-limiting step, in agreement with an earlier study (7). In contrast, the destaining rates of different dyes would be expected to be similar during full fusion. In previous studies, the destaining rates of different FM dyes (e.g., FM1–84, FM1–43, and FM2–10) from pre-synaptic boutons were reported to differ (1) or to be the same (26). The reasons for these apparent discrepancies remain to be resolved. A recent study - using quantum dots - provides strong support for the notion that kiss-and-run exocytosis is a common mode of transmitter release in hippocampal neurons (23). According to this new study, the fraction of kiss-and-run versus full fusion events is subject to regulation; under specific conditions, one mode of exocytosis is predominant over the other one, but whether kiss-and-run predominates at high or low stimulation frequencies is still an open question (18, 57).

There are indications that the diameter of SV fusion pores in the calyx of Held synapse are >2.3 nm, and a small fraction are ~ 1.1 nm (19). However, fusion pores that mediate exocytosis from microvesicles in posterior pituitary nerve terminals have been reported to have a diameter of only 0.6 nm (2), which is too small to take up or release dyes during kiss-and-run exocytosis and thus would elude detection in FM dye experiments. The diameters cited above were derived from conductance measurements obtained by capacitance experiments. This approach is not amenable to study modes of exocytosis in central neurons with tiny boutons. So, in most cases, the frequency of kiss-and-run, and the diameter of fusion pores, remain unknown. Hence, it is difficult to estimate the rate of neurotransmitter flux during kiss-and-run exocytosis. This is a crucial question because, again, small pores might retard efflux of glutamate, for example, resulting in receptor desensitization rather than activation (8). To gain insight into the structure and properties of fusion pores in central neurons, a detailed understanding of dye loss from SVs and from model systems is needed. The data reported here help to provide an empirical basis to interpret dye destaining data from single SVs.

Two general hypothetical models of fusion pore structure - the lipidic pore and the protein-lined pore - have been proposed (13, 27). Han et al., using amperometry and capacitance measurements to study large dense core vesicle secretion in PC12 cells, suggest that the fusion pore is transiently lined by the transmembrane domains of multiple syntaxin molecules (34), which is a soluble N-ethylmaleimide-sensitive factor attachment protein receptor (SNARE) that, together with SNAP-25 and synaptobrevin, forms the core of the fusion machinery (58, 59). Trp mutations at three sites of the transmembrane domain of syntaxin decreased the flux of transmitter and the conductance of fusion pores, and would thus be predicted to retard the rate of FM dye loss from vesicles, or even prevent dye permeation during kiss-and-run events. It will therefore be of interest to analyze the rate of dye release from vesicles undergoing exocytosis in PC12 cells to gain further insight into the structure of biological fusion pores; indeed, ~ one quarter of release events in PC12 cells occur via a kiss-and-run mechanism (12). It will also be interest to determine whether Trp mutations in the cognate v-SNARE protein, synaptobrevin, which is anchored in the vesicle membrane, retard dye efflux; if so, it would strongly suggest that synaptobrevin forms the other half of the fusion pore. A long term goal will be to use the same approach to test the "SNARE-lined pore model" during kiss-and-run SV exocytosis in neurons.

Supplementary Material

Refer to Web version on PubMed Central for supplementary material.

Acknowledgments

We thank F. Mao for providing SynptoGreen C3 and SGC5, and M. Jackson and the Chapman lab for helpful discussions. We also thank Guanhua Hou for carrying out the estimations of dye diameters.

FUNDING SOURCES: This work was supported by grants from the NIH (MH 61876 to E.R.C. and GM071428/GM084028 to Q.C.). E.R.C is an Investigator of the Howard Hughes Medical Institute. Computational resources were from the National Center for Supercomputing Applications (NCSA) Alliance center at the University of Illinois. H. Bayley acknowledges support through the Royal Society-Wolfson Research Merit Award and the Medical Research Council.

ABBREVIATIONS

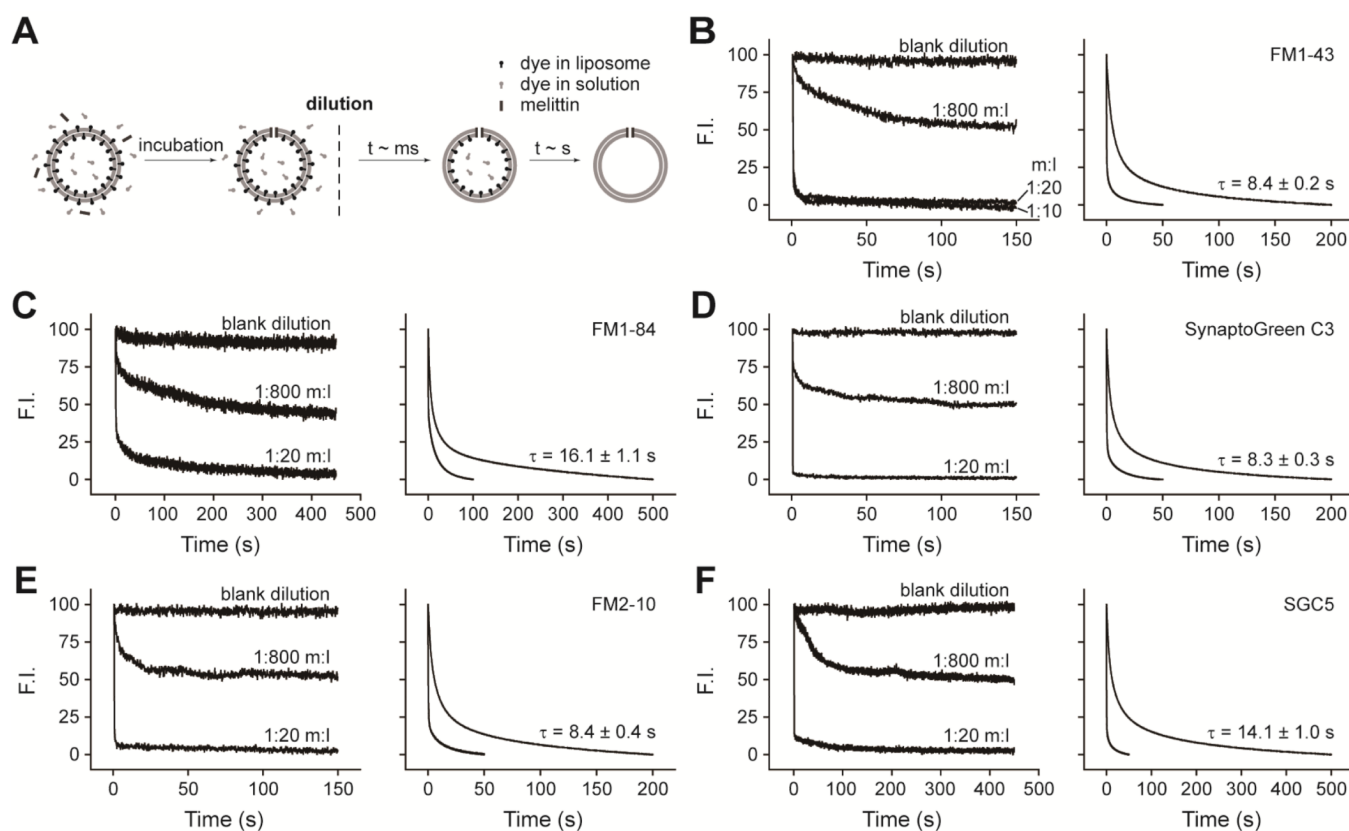
PC	1,2-dioleoyl-sn-glycero-3-phosphocholine
PE	1,2-dioleoyl-sn-glycero-3-phosphoethanolamine
αHL	α -hemolysin
αHL-M113W	M113W mutant form of α HL
αHL-wt	wild-type α HL
COM	center of mass
GLE	Generalized Langevin Equation
LDCV	large dense-core vesicle
MD	molecular dynamics
SNARE	soluble N-ethylmaleimide-sensitive factor attachment protein receptor
SV	synaptic vesicle
Trp	tryptophan
WHAM	Weighted Histogram Analysis Method

REFERENCES

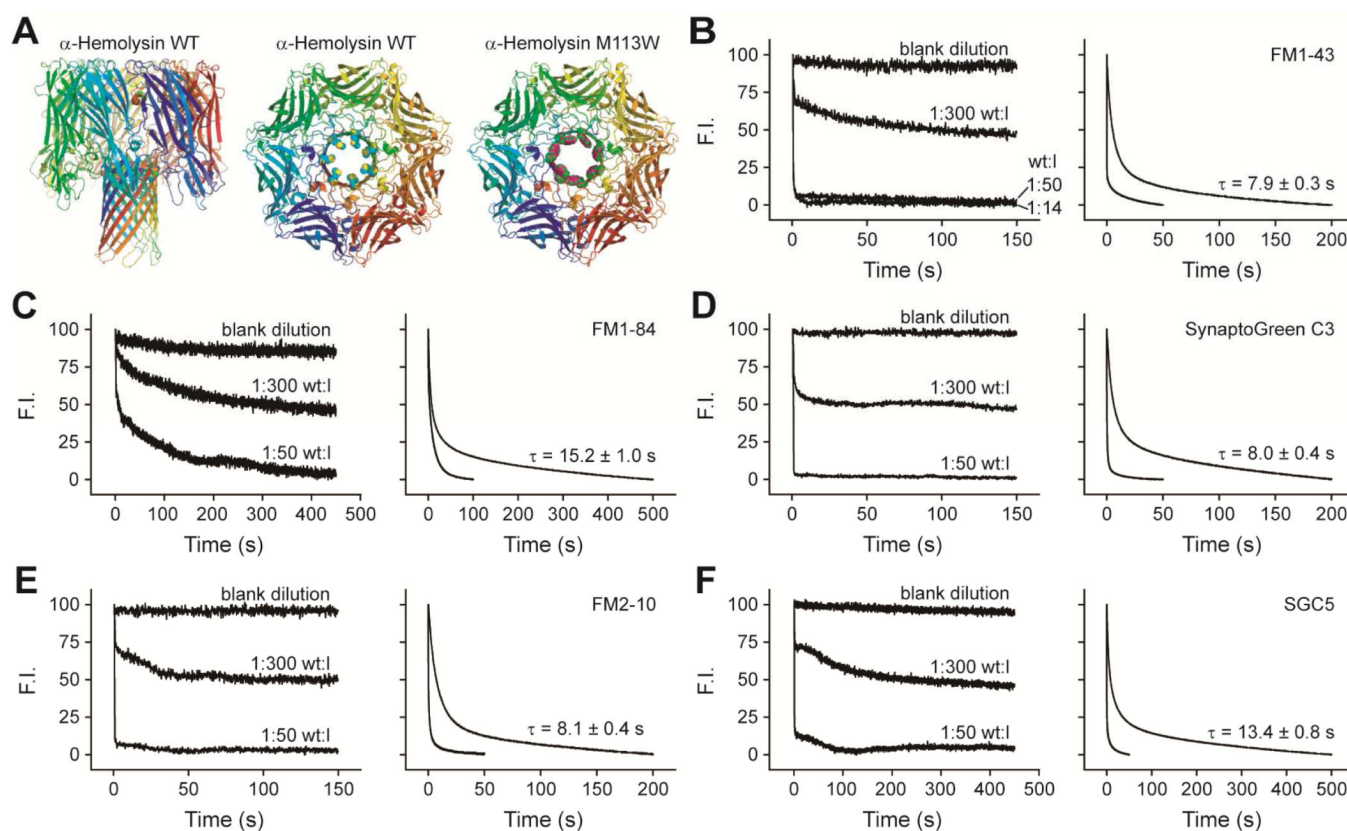
1. Klingauf J, Kavalali ET, Tsien RW. Kinetics and regulation of fast endocytosis at hippocampal synapses. *Nature*. 1998; 394:581–585. [PubMed: 9707119]
2. Klyachko VA, Jackson MB. Capacitance steps and fusion pores of small and large-dense-core vesicles in nerve terminals. *Nature*. 2002; 418:89–92. [PubMed: 12097912]
3. Neher E, Marty A. Discrete changes of cell membrane capacitance observed under conditions of enhanced secretion in bovine adrenal chromaffin cells. *Proc Natl Acad Sci U S A*. 1982; 79:6712–6716. [PubMed: 6959149]
4. Wang CT, Lu JC, Bai J, Chang PY, Martin TF, Chapman ER, Jackson MB. Different domains of synaptotagmin control the choice between kiss-and-run and full fusion. *Nature*. 2003; 424:943–947. [PubMed: 12931189]
5. Heuser JE, Reese TS. Evidence for recycling of synaptic vesicle membrane during transmitter release at the frog neuromuscular junction. *J Cell Biol*. 1973; 57:315–344. [PubMed: 4348786]
6. Fesce R, Grohovaz F, Valtorta F, Meldolesi J. Neurotransmitter release: fusion or 'kiss-and-run'? *Trends Cell Biol*. 1994; 4:1–4. [PubMed: 14731821]
7. Richards DA, Bai J, Chapman ER. Two modes of exocytosis at hippocampal synapses revealed by rate of FM1–43 efflux from individual vesicles. *J Cell Biol*. 2005; 168:929–939. [PubMed: 15767463]
8. Richards DA. Vesicular release mode shapes the postsynaptic response at hippocampal synapses. *J Physiol*. 2009; 587:5073–5080. [PubMed: 19752123]
9. Fulop T, Radabaugh S, Smith C. Activity-dependent differential transmitter release in mouse adrenal chromaffin cells. *J Neurosci*. 2005; 25:7324–7332. [PubMed: 16093382]
10. Albillos A, Dernick G, Horstmann H, Almers W, Alvarez de Toledo G, Lindau M. The exocytotic event in chromaffin cells revealed by patch amperometry. *Nature*. 1997; 389:509–512. [PubMed: 9333242]
11. Alvarez de Toledo G, Fernandez-Chacon R, Fernandez JM. Release of secretory products during transient vesicle fusion. *Nature*. 1993; 363:554–558. [PubMed: 8505984]
12. Wang CT, Bai J, Chang PY, Chapman ER, Jackson MB. Synaptotagmin-Ca²⁺ triggers two sequential steps in regulated exocytosis in rat PC12 cells: fusion pore opening and fusion pore dilation. *J Physiol*. 2006; 570:295–307. [PubMed: 16293646]
13. Lindau M, Almers W. Structure and function of fusion pores in exocytosis and ectoplasmic membrane fusion. *Curr Opin Cell Biol*. 1995; 7:509–517. [PubMed: 7495570]
14. Lollike K, Borregaard N, Lindau M. The exocytotic fusion pore of small granules has a conductance similar to an ion channel. *J Cell Biol*. 1995; 129:99–104. [PubMed: 7535305]
15. Fernandez JM, Neher E, Gomperts BD. Capacitance measurements reveal stepwise fusion events in degranulating mast cells. *Nature*. 1984; 312:453–455. [PubMed: 6504157]
16. Chen X, Barg S, Almers W. Release of the styryl dyes from single synaptic vesicles in hippocampal neurons. *J Neurosci*. 2008; 28:1894–1903. [PubMed: 18287506]
17. Aravanis AM, Pyle JL, Tsien RW. Single synaptic vesicles fusing transiently and successively without loss of identity. *Nature*. 2003; 423:643–647. [PubMed: 12789339]
18. Gandhi SP, Stevens CF. Three modes of synaptic vesicular recycling revealed by single-vesicle imaging. *Nature*. 2003; 423:607–613. [PubMed: 12789331]
19. He L, Wu XS, Mohan R, Wu LG. Two modes of fusion pore opening revealed by cell-attached recordings at a synapse. *Nature*. 2006; 444:102–105. [PubMed: 17065984]
20. Granseth B, Odermatt B, Royle SJ, Lagnado L. Clathrin-mediated endocytosis is the dominant mechanism of vesicle retrieval at hippocampal synapses. *Neuron*. 2006; 51:773–786. [PubMed: 16982422]
21. Spruce AE, Breckenridge LJ, Lee AK, Almers W. Properties of the fusion pore that forms during exocytosis of a mast cell secretory vesicle. *Neuron*. 1990; 4:643–654. [PubMed: 2344404]
22. Zhu Y, Xu J, Heinemann SF. Two pathways of synaptic vesicle retrieval revealed by single-vesicle imaging. *Neuron*. 2009; 61:397–411. [PubMed: 19217377]

23. Zhang Q, Li Y, Tsien RW. The dynamic control of kiss-and-run and vesicular reuse probed with single nanoparticles. *Science*. 2009; 323:1448–1453. [PubMed: 19213879]
24. Betz WJ, Mao F, Bewick GS. Activity-dependent fluorescent staining and destaining of living vertebrate motor nerve terminals. *J Neurosci*. 1992; 12:363–375. [PubMed: 1371312]
25. Wu Y, Yeh FL, Mao F, Chapman ER. Biophysical characterization of styryl dye-membrane interactions. *Biophys J*. 2009; 97:101–109. [PubMed: 19580748]
26. Fernandez-Alfonso T, Ryan TA. The kinetics of synaptic vesicle pool depletion at CNS synaptic terminals. *Neuron*. 2004; 41:943–953. [PubMed: 15046726]
27. Jackson MB, Chapman ER. Fusion pores and fusion machines in Ca^{2+} -triggered exocytosis. *Annu Rev Biophys Biomol Struct*. 2006; 35:135–160. [PubMed: 16689631]
28. Breckenridge LJ, Almers W. Currents through the fusion pore that forms during exocytosis of a secretory vesicle. *Nature*. 1987; 328:814–817. [PubMed: 2442614]
29. Debus K, Lindau M. Resolution of patch capacitance recordings and of fusion pore conductances in small vesicles. *Biophys J*. 2000; 78:2983–2997. [PubMed: 10827977]
30. Yang L, Harroun TA, Weiss TM, Ding L, Huang HW. Barrel-stave model or toroidal model? A case study on melittin pores. *Biophys J*. 2001; 81:1475–1485. [PubMed: 11509361]
31. Matsuzaki K, Yoneyama S, Miyajima K. Pore formation and translocation of melittin. *Biophys J*. 1997; 73:831–838. [PubMed: 9251799]
32. van den Bogaart G, Mika JT, Krasnikov V, Poolman B. The lipid dependence of melittin action investigated by dual-color fluorescence burst analysis. *Biophys J*. 2007; 93:154–163. [PubMed: 17434946]
33. Rex S. Pore formation induced by the peptide melittin in different lipid vesicle membranes. *Biophys Chem*. 1996; 58:75–85. [PubMed: 8679920]
34. Han X, Wang CT, Bai J, Chapman ER, Jackson MB. Transmembrane segments of syntaxin line the fusion pore of Ca^{2+} -triggered exocytosis. *Science*. 2004; 304:289–292. [PubMed: 15016962]
35. Song L, Hobaugh MR, Shustak C, Cheley S, Bayley H, Gouaux JE. Structure of staphylococcal alpha-hemolysin, a heptameric transmembrane pore. *Science*. 1996; 274:1859–1866. [PubMed: 8943190]
36. Cheley S, Malghani MS, Song L, Hobaugh M, Gouaux JE, Yang J, Bayley H. Spontaneous oligomerization of a staphylococcal alpha-hemolysin conformationally constrained by removal of residues that form the transmembrane beta-barrel. *Protein Eng*. 1997; 10:1433–1443. [PubMed: 9543005]
37. Gu LQ, Cheley S, Bayley H. Prolonged residence time of a noncovalent molecular adapter, beta-cyclodextrin, within the lumen of mutant alpha-hemolysin pores. *J Gen Physiol*. 2001; 118:481–494. [PubMed: 11696607]
38. Brunger AT, Karplus M. Polar hydrogen positions in proteins: empirical energy placement and neutron diffraction comparison. *Proteins*. 1988; 4:148–156. [PubMed: 3227015]
39. Brooks BR, Bruccoleri RE, Olafson BD, States DJ, Swaminathan S, Karplus M. Charmm - a program for macromolecular energy, minimization, and dynamics calculations. *J Comput. Chem*. 1983; 4:187–217.
40. MacKerell AD, Bashford D, Bellott M, Dunbrack RL, Evanseck JD, Field MJ, Fischer S, Gao J, Guo H, Ha S, Joseph-McCarthy D, Kuchnir L, Kuczera K, Lau FTK, Mattos C, Michnick S, Ngo T, Nguyen DT, Prodhom B, Reiher WE, Roux B, Schlenkrich M, Smith JC, Stote R, Straub J, Watanabe M, Wiorkiewicz-Kuczera J, Yin D, Karplus M. All-atom empirical potential for molecular modeling and dynamics studies of proteins. *J. Phys. Chem. B*. 1998; 102:3586–3616.
41. Ryckaert JP, Ciccotti G, Berendsen HJC. Numerical-integration of cartesian equations of motion of a system with constraints - molecular-dynamics of n-alkanes. *J. Comput. Phys*. 1977; 23:327–341.
42. Beglov D, Roux B. Finite representation of an infinite bulk system - solvent boundary potential for computer-simulations. *J. Chem. Phys*. 1994; 100:9050–9063.
43. Im W, Berneche S, Roux B. Generalized solvent boundary potential for computer simulations. *J. Chem. Phys*. 2001; 114:2924–2937.
44. Im WP, Lee MS, Brooks CL. Generalized born model with a simple smoothing function. *J. Comput. Chem*. 2003; 24:1691–1702. [PubMed: 12964188]

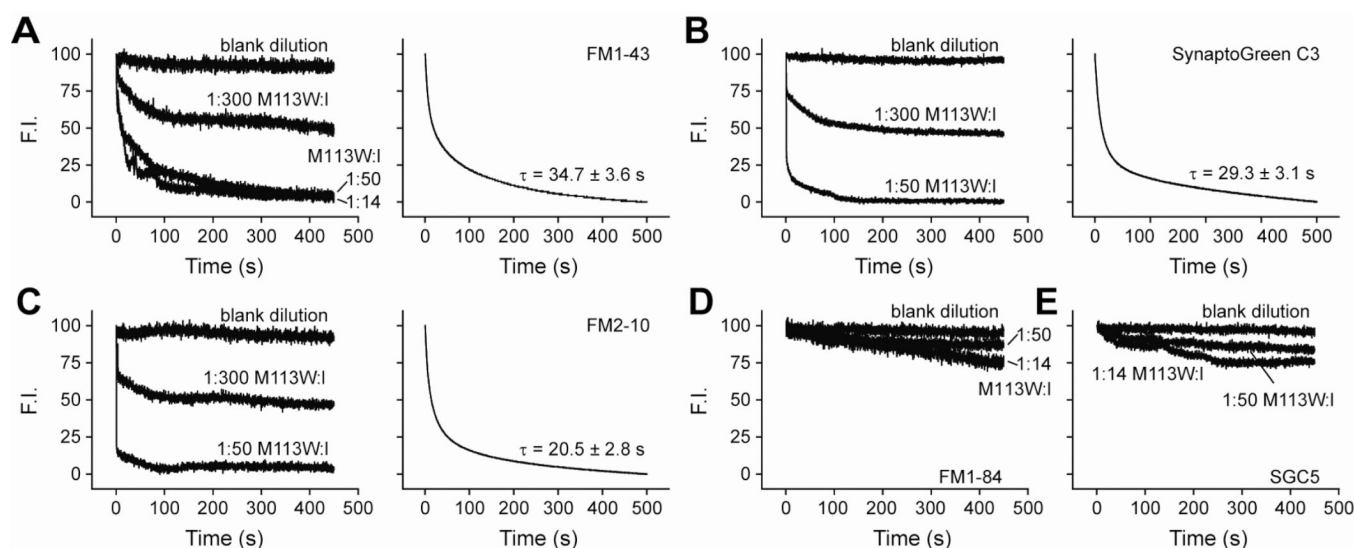
45. Jorgensen WL, Chandrasekhar J, Madura JD, Impey RW, Klein ML. Comparison of simple potential functions for simulating liquid water. *J. Chem. Phys.* 1983; 79:926–935.
46. Nina M, Beglov D, Roux B. Atomic radii for continuum electrostatics calculations based on molecular dynamics free energy simulations. *J. Phys. Chem. B.* 1997; 101:5239–5248.
47. Nina M, Im W, Roux B. Optimized atomic radii for protein continuum electrostatics solvation forces. *Biophysical Chemistry.* 1999; 78:89–96. [PubMed: 17030305]
48. Hoover WG. Canonical dynamics - equilibrium phase-space distributions. *Phys. Rev. A.* 1985; 31:1695–1697. [PubMed: 9895674]
49. Nose S. A unified formulation of the constant temperature molecular-dynamics methods. *J. Chem. Phys.* 1984; 81:511–519.
50. Elstner M, Porezag D, Jungnickel G, Elsner J, Haugk M, Frauenheim T, Suhai S, Seifert G. Self-consistent-charge density-functional tight-binding method for simulations of complex materials properties. *Physical Review B.* 1998; 58:7260–7268.
51. Kumar S, Bouzida D, Swendsen RH, Kollman PA, Rosenberg JM. The weighted histogram analysis method for free-energy calculations on biomolecules. I. The method. *J. Comput. Chem.* 1992; 13:1011–1021.
52. Kumar S, Rosenberg JM, Bouzida D, Swendsen RH, Kollman PA. Multidimensional free-energy calculations using the weighted histogram analysis method. *J. Comput. Chem.* 1995; 16:1339–1350.
53. Lifson S, Jackson JL. On the self-diffusion of ions in a polyelectrolyte solution. *J. Chem. Phys.* 1962; 36:2410–2414.
54. Zwanzig R. Diffusion in a rough potential. *Proc. Nat. Acad. Sci. USA.* 1988; 85:2029–2030. [PubMed: 3353365]
55. Roux B, Allen T, Berneche S, Im W. Theoretical and computational models of biological ion channels. *Quart. Rev. Biophys.* 2004; 37:15–103.
56. Menestrina G. Ionic channels formed by *Staphylococcus aureus* alpha-toxin: voltage-dependent inhibition by divalent and trivalent cations. *J Membr Biol.* 1986; 90:177–190. [PubMed: 2425095]
57. Harata NC, Choi S, Pyle JL, Aravanis AM, Tsien RW. Frequency-dependent kinetics and prevalence of kiss-and-run and reuse at hippocampal synapses studied with novel quenching methods. *Neuron.* 2006; 49:243–256. [PubMed: 16423698]
58. Weber T, Zemelman BV, McNew JA, Westermann B, Gmachl M, Parlati F, Sollner TH, Rothman JE. SNAREpins: minimal machinery for membrane fusion. *Cell.* 1998; 92:759–772. [PubMed: 9529252]
59. Sollner T, Bennett MK, Whiteheart SW, Scheller RH, Rothman JE. A protein assembly-disassembly pathway in vitro that may correspond to sequential steps of synaptic vesicle docking, activation, and fusion. *Cell.* 1993; 75:409–418. [PubMed: 8221884]
60. Humphrey W, Dalke A, Schulten K. VMD: visual molecular dynamics. *J Mol Graph.* 1996; 14:33–38. 27–38. [PubMed: 8744570]

**FIGURE 1.**

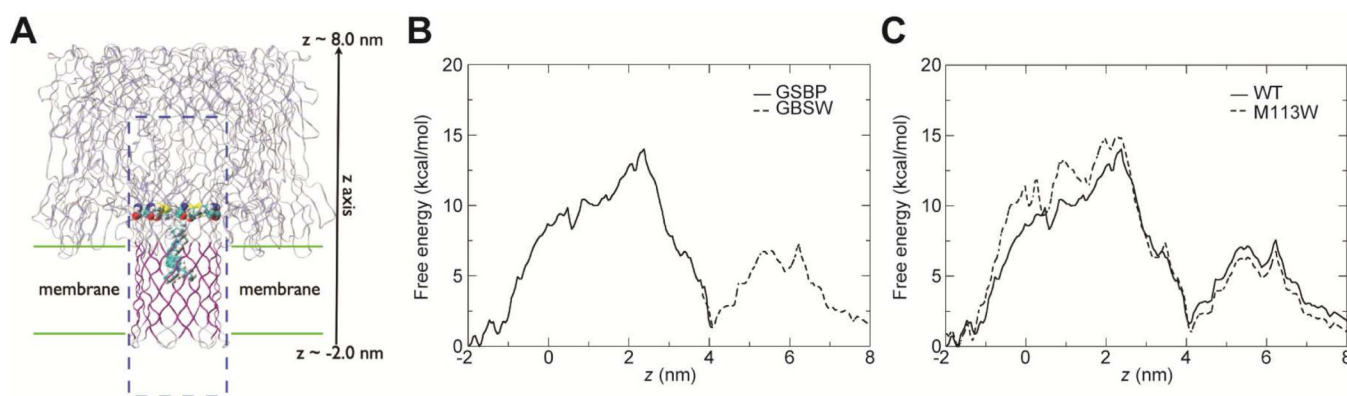
Efflux of dyes through melittin pores. (A) Outline of the experimental procedure used to monitor dye efflux from liposomes. (B–F) Left panels: sample traces from the hand-mixing experiments showing FM1–43, FM1–84, SynaptoGreen C3, FM2–10, and SGC5 efflux through fully assembled melittin pores. The ‘blank dilution’ trace indicates samples that were diluted in the absence of pore forming toxin. The molar ratios of melittin/lipid (m:l) were 1:800, 1:20, and 1:10. F.I. denotes fluorescence intensity in arbitrary units. (B–F) Right panels: dye efflux was time-resolved using a rapid mixing stopped-flow instrument. The upper traces and lower traces are from samples with a 1:800 and a 1:20 m:l ratio, respectively. τ values are the mean \pm SE from three separate experiments. All kinetic traces were normalized.

**FIGURE 2.**

Efflux of dyes through α HL-wt pores. (A) Structures of wild type and M113W mutant α HL. From left to right: side view of α HL-wt; top view of α HL-wt with methionine residues at position 113 shown in space fill; top view of α HL-M113W where tryptophan residues at position 113 are shown in space fill. Images for these structures were generated using PyMOL software. (B–F) Efflux of dyes from fully assembled α HL-wt pores from hand-mixing (Left panels) and rapid mixing stopped-flow experiments (Right panels) as described in Figure 1. In the rapid mixing experiments, the upper trace and lower traces harbor wild type toxin:lipid (wt:l) ratios of 1:300 and 1:50, respectively. τ values are the mean \pm SE from three separate experiments.

**FIGURE 3.**

Efflux of dyes through α HL-M113W pores. (A–C) Efflux of FM1–43, SynaptoGreen C3, and FM2–10 from fully assembled α HL-M113W pores measured via hand-mixing experiments (Left panels) and rapid mixing stopped-flow experiments (Right panels) as described in Figure 1. In the rapid mixing experiments, the molar ratios of mutant toxin:lipid (M113W:I) were 1:300 (upper traces) and 1:50 (lower traces). τ values are the mean \pm SE from three separate determinations. (D–E) Hand mixing experiments revealed that FM1–84 and SGC5 cannot pass through fully assembled α HL-M113W pores at M113W:I ratios of 1:50 and 1:14.

**FIGURE 4.**

Simulation setup and free energy profiles. (A) A snapshot of wild-type α HL. The protein is shown in the ribbon form and the transmembrane region is shown in purple. M113 and an FM1-43 molecule are shown in the van der Waals scheme. The water solvation box for the GSBP setup is shown in the box bounded by the blue dashed lines with water molecules omitted for clarity. The figure is made using VMD (60). (B) Comparison of free energy profiles $W(z)$ for FM1-43 diffusing through α HL-wt using two methods, GSBP and GBSW, which generate consistent $W(z)$ in the overlapping region z between 3.8 and 4.1 nm. (C) Computed free energy profiles $W(z)$ of FM1-43 for the translocation of FM1-43 in both α HL-wt (solid line) and α HL-M113W (dashed line) based on umbrella sampling simulations.

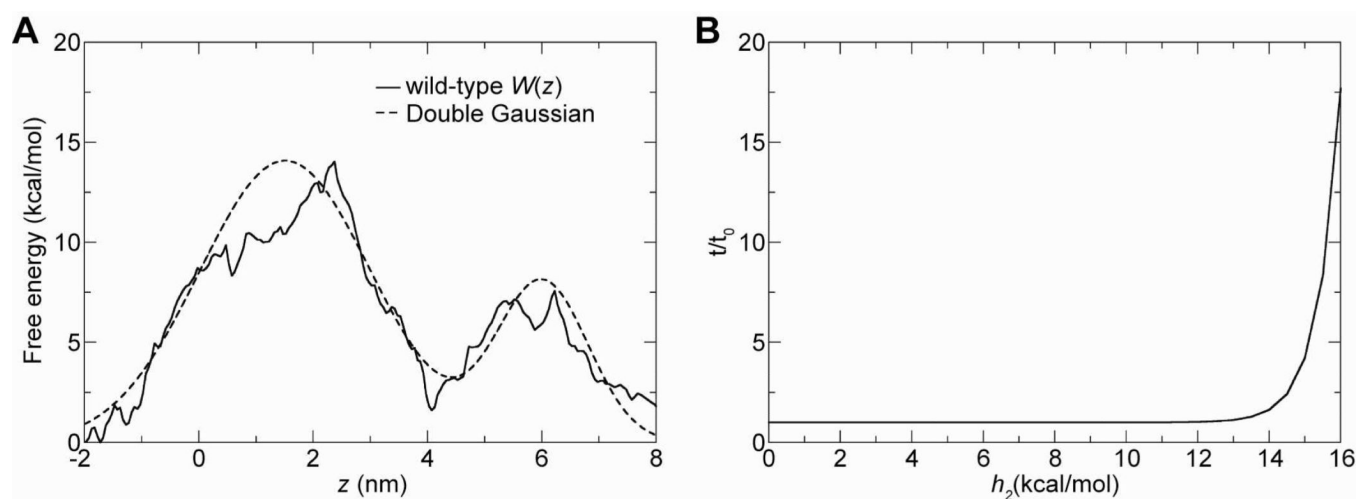


FIGURE 5.

The insensitivity of t to the second lower barrier. (A) Fitting $W(z)$ for α HL-wt with a double Gaussian function as given in Eq. 2. The double Gaussian function gives the same translocation time as the wild-type $W(z)$. (B) The ratio t/t_0 for the double Gaussian function as a function of h_2 with fixed $h_1=14.08$ kcal/mol.

TABLE 1

Efflux time constants from nanometer pores

	FM 1-84	FM 1-43	SGC3*	FM 2-10	SGC5
	<i>S</i>	<i>S</i>	<i>S</i>	<i>S</i>	<i>S</i>
Melittin	16.1 ± 1.1	8.4 ± 0.2	8.3 ± 0.3	8.4 ± 0.4	14.1 ± 1.0
αHL-wt	15.2 ± 1.0	7.9 ± 0.3	8.0 ± 0.4	8.1 ± 0.4	13.4 ± 0.8
αHL-M113W	--	34.7 ± 3.6	29.3 ± 3.1	20.5 ± 2.8	--

* SGC3: SynaptoGreen C3